Low-Thrust Earth-Moon Transfer Trajectories to Stable Distant Retrograde Orbits using Indirect Optimization Method

75th International Astronautical Congress (IAC), Milan, Italy, 14-18 October 2024.

IAC-24-A3.IP.139.x89091

Low-Thrust Earth-Moon Transfer Trajectories to Stable Distant Retrograde Orbits using Indirect Optimization Method

Daniele Pice[1]*, Luigi Mascolo[2], Manuela Battipede[3]

Dipartimento di Ingegneria Meccanica e Aerospaziale, Politecnico di Torino, 24 Corso Duca degli Abruzzi, 10129 Turin, Italy

* Corresponding Author
✉ [1]danielepice99@gmail.com, [2]luigi.mascolo@polito.it, [3]manuela.battipede@polito.it

Abstract

This research focuses on identifying low-thrust optimal trajectories for inserting satellites into a Distant Retrograde Orbit (DRO) around the Moon with minimum propellant usage, contributing to cost-effective strategies and enabling heavier payloads for future cislunar missions. This study is motivated by the growing interest in establishing a scientific presence in cislunar space, with initiatives aiming to position orbital stations on such orbits, or to utilize lunar resources and create a launchpad for missions to Mars and beyond. NASA's Artemis program is heading in this direction. Among potential locations, Periodic Orbits around Lagrangian Points, including DROs and Near-Rectilinear Halo Orbits (NRHOs), present promising options. DROs, in particular, offer significant advantages due to their stability, reducing maintenance costs and prolonging mission lifespans. To optimize DRO insertion trajectories, a Two-Point Boundary Value Problem approach is employed. This method enhances solution convergence amid the chaotic gravitational dynamics between Earth and the Moon and includes an iterative shooting procedure with a bang-bang thrust control law derived from indirect optimal control theory. Pontryagin's Maximum Principle is applied to ensure the optimality of control solutions. DRO computations are performed within the Circular Restricted Three-Body Problem (CR3BP) framework using a single-shooting method based on the State Transition Matrix analysis. This model accounts for the gravitational influences of the Moon, which significantly impacts both the injection trajectory and the stability of the DRO. Results indicate that two-burn finite-thrust trajectories present the most efficient means for direct DRO insertion from Earth, effectively exploiting the Earth-Moon gravitational interaction without the need of performing a lunar gravity assist or multiple swing-bys. The optimal trajectory has proven to be the one that best fits the shape of the orbit, inserting the satellite directly into the final stable DRO.

Keywords: Distant Retrograde Orbit • Indirect Optimization • Low-Thrust Lunar Transfer • Direct Insertion • Circular Restricted Three-Body Problem

1. Introduction

DROs are a specific class of Periodic Orbits (POs) in the Earth-Moon three-body system, which combine a retrograde motion, opposite to the Moon's orbiting direction, and large amplitudes. In more general terms, these orbits can be centered in the secondary attractor of any CR3BP, of which they represent a closed-form solution.

As early as 1968, Broucke provided initial evidence of the existence of DROs within the CR3BP [1]. Further investigations into DROs are attributed to Hénon [2-6], focusing on the specific Hill's Case model derived from the broader CR3BP framework. In such scenario, Hénon treated different POs families numerically, investigating their generation and stability properties. Nonetheless, the term *Distant Retrograde Orbit* was apparently coined by Ocampo and Rosborough only twenty-five years later, in 1993 [7]. As regards the Earth-Moon system, Whitley and Martinez have compared various types of POs as potential staging orbits in cislunar space [8]. Among the examined options, only NRHOs and DROs have proven to be feasible, due to their high accessibility and minimal eclipse periods. DROs, specifically, exhibit a multi-years stability, due to the interactions with Lagrangian points L1 and L2, so that no corrective maneuvers are required. Their general stability has been formally studied in [9, 10]. These unique properties have led DROs to be rediscovered in recent years, paving the way for more in-depth analyses and promising mission concepts. In 2011, NASA proposed the Asteroid Redirect Mission (ARM), intended to visit a large near-Earth asteroid for collecting samples, by exploiting DROs' stability [11]. Unfortunately, the mission was canceled in 2017. Notably, DROs was even considered as a cost-effective alternative to NRHOs for stationing the future Lunar Orbital Platform-Gateway (LOP-G).

Among all the proposed missions involving DROs, NASA's Artemis I stands out as the only one that has been developed and completed [12]. Launched in 2022,

this uncrewed mission served as a testing flight of the Orion spacecraft and Space Launch System rocket (SLS) in preparation for subsequent Artemis missions. After separation from the upper stage, the capsule performed a trans-lunar injection on a Moon-centered DRO, flew-by around the Moon, and then returned to Earth [13]. The Orion spent a total of three weeks in space, 6 days of which on orbit, approaching approximately to a distance of 130 km from the lunar surface. Further details on mission design and a complete optimization analysis of the Artemis I trajectory are given in [14, 15].

In literature, several works have investigated how to exploit DROs as low-energy transfer orbits in the Earth-Moon CR3BP [16, 17]. Indeed, it is possible to study their dynamical evolution and leverage the manifolds for maneuvering at much lower costs compared to traditional operations in the Keplerian model [18, 19]. Various mission scenarios for a transfer to DROs are explored in [20]; these solutions for DRO insertion range from exploiting the adjacent Lyapunov orbits at L1 and L2 to performing a powered lunar fly-by (exactly like Artemis I) or even undertaking a more complex direct transfer. Recent contributions have directly analyzed a transfer from an initial parking DRO to Low Lunar Orbits [21]. A diverse concept is proposed in [22], where a LEO-to-DRO transfer is coupled with a rendezvous maneuver on lunar orbits for future space outposts or supply stations. Conte, moreover, examines DROs as support trajectories for refueling during deeper space missions [23, 24].

This paper fits perfectly with the described framework, focusing on the optimization of direct transfer trajectories to a lunar DRO within the CR3BP model. The analysis relies on the indirect formulation leveraging the fundamentals of the Optimal Control Theory (OCT). Specifically, a single-shooting algorithm based on Newton's method is implemented, assuming a *bang-bang* thrust control strategy. The Pontryagin's Maximum Principle (PMP) is adopted to ensure the optimality of solutions.

2. Background

As anticipated, the examined scenario involves an Earth-to-Moon transfer trajectory, followed by a direct insertion into a Moon-centered DRO. The aim is to identify the optimal trajectory at minimum propellant request that fulfills all boundary conditions. First off, such DRO has to be generated; the abovementioned shooting procedure allows to compute a completely closed orbit in the CR3BP, then targeted as final condition for the actual optimization process.

2.1 Dynamical model

The CR3BP model is adopted, which, under specific assumptions, is sufficient to set the stage for understanding the essential dynamics of a spacecraft in a multi-body gravitational scenario.

Considering the Earth-Moon binary system, this simplified model implies the presence of two main bodies, with parameters μ_1 and μ_2 respectively for the Earth and the Moon, revolving around their barycenter and a third body representing the spacecraft. As a fundamental hypothesis, the third mass is smaller than the primaries, so its gravitational contribution is assumed negligible [25].

The full set of problem governing ODEs, including the mass equation, can be written as follows [26]:

$$\begin{aligned} \dot{\boldsymbol{r}} &= \boldsymbol{V} \\ \dot{\boldsymbol{V}} &= \boldsymbol{g}(\boldsymbol{r}) + \boldsymbol{h}(\boldsymbol{V}) + \frac{\boldsymbol{T}}{m} \\ \dot{m} &= -\frac{T}{c}, \end{aligned} \tag{1}$$

where $\boldsymbol{r} = \{x, y, z\}^T$, $\boldsymbol{V} = \{\dot{x}, \dot{y}, \dot{z}\}^T$, and $\boldsymbol{T}$ are respectively the position, velocity, and thrust vectors, m is the mass of the spacecraft, and c is the exhaust velocity. The functions $\boldsymbol{g}(\boldsymbol{r})$ and $\boldsymbol{h}(\boldsymbol{V})$ are introduced to compact the equations:

$$\boldsymbol{g}(\boldsymbol{r}) = \begin{bmatrix} \partial U/\partial x \\ \partial U/\partial y \\ \partial U/\partial z \end{bmatrix} \tag{2}$$

$$\boldsymbol{h}(\boldsymbol{V}) = \begin{bmatrix} 2\dot{y} \\ -2\dot{x} \\ 0 \end{bmatrix}. \tag{3}$$

The effective potential U is given by:

$$U = \frac{1-\mu}{r_{13}} + \frac{\mu}{r_{23}} + \frac{1}{2}(x^2 + y^2) + \frac{1}{2}\mu(1-\mu), \tag{4}$$

where $\mu = \mu_2/(\mu_1 + \mu_2)$ is the mass ratio, while r_{13} and r_{23} correspond to the distances between spacecraft and primaries, expressed as $r_{i3} = [(x - x_i)^2 + y^2 + z^2]^{1/2}$, for $i = 1, 2$. All these equations follow the classical nondimensionalization of the CR3BP. The physical parameters and the reference quantities used in this analysis are listed in Table 1.

Since the CR3BP equations of motion are autonomous, there is a sole, consistent pseudo-integral of motion that is conserved, namely the Jacobi constant:

$$C = 2U - (\dot{x}^2 + \dot{y}^2 + \dot{z}^2). \tag{5}$$

Such energy-like quantity, sum of the kinetic and potential contributions, is invaluable for planning space mission trajectories and analyzing orbital stability as it allows to investigate which regions are accessible to the spacecraft and identify areas where escapes or collisions are not possible under the CR3BP assumptions. These regions are delineated by the Zero-Velocity Surfaces (ZVS), boundaries where the energy is entirely potential and cannot be exceeded without any additional energy.

Table 1. Physical parameters adopted for the analysis.

Symbol	Value	Unit	Meaning
μ_E	3.98600442×10^5	km^3/s^2	Earth gravitational parameter
μ_M	4.90280108×10^3	km^3/s^2	Moon gravitational parameter
r_E	6.37813630×10^3	km	Earth mean radius
r_M	1.73700000×10^3	km	Moon mean radius
R	3.84400000×10^4	km	Distance Unit
τ	4.34247985	day	Time Unit

2.2 Distant Retrograde Orbits

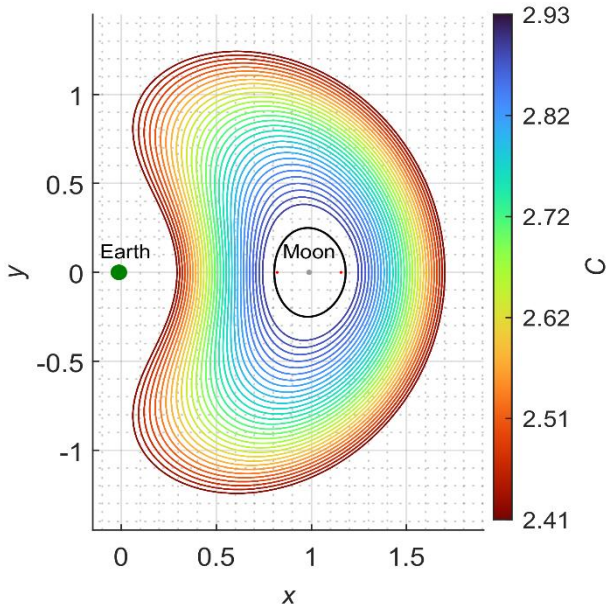

Fig. 1. DRO family

Analyzing several POs families in the Earth-Moon system, Hénon identified specific selenocentric POs characterized by a quasi-elliptical shape and very large radii with respect the closest primary (i.e. the Moon). DROs are indeed *distant* as they are situated at significant distances from the Moon, with medium radii extending tens of thousands of kilometers from the lunar surface. Furthermore, these orbits exhibit a retrograde rotating motion, orbiting in the opposite direction to the Moon's trajectory. Such unique geometry, combined with their relative position within the Earth-Moon gravitational field, contributes to a high level of stability, leading DROs to be classified in the Hénon family *f* [3].

Unlike orbits near L1 and L2, which are sensitive to small perturbations and require constant corrections to remain stable, DROs pass above these points at a greater distance, avoiding stability issues and maintaining their trajectory over time. These properties make DROs perfect solutions for long-term space missions, such as Earth or Moon observation missions, where frequent orbital corrections are typically required. However, DROs are stable when only planar motion is considered; a change in stability can signal various bifurcations with other families of POs, even three-dimensional ones.

Here, DROs are generated starting from their adjacent Lyapunov Orbits (LOs), centered in L2 [27]. The planar bifurcation from LOs, indeed, occurs when the tangential velocity $\dot{y}$ increases to such an extent as to produce orbits with greater amplitudes and lower Jacobi constants, capable of exceeding even L1. In particular, the orbits are computed by implementing a single-shooting method with a Richardson correction of the third order [28].

By vaguely taking the Artemis I mission orbit as reference, a DRO with an average radius of $\approx 83{,}000$ km is considered. The main characteristics of this DRO, which serves as foundation for the optimization procedure, are provided below. Figure 1 shows the entire DRO family, represented in the Earth-Moon binary system. The orbit in black is exactly the DRO under investigation, from which the other orbits, classified as a function of Jacobi integral, are propagated.

Table 2. DRO characteristic properties.

Property	Value	Unit
Perilune	70392.55	km
Apolune	96058.13	km
Period	14.00	day

2.3 Mass optimization problem

Based on the OCT, the problem is stated as a classical TPBVP, by coupling the system governing ODEs and the boundary conditions, all grouped in the constraint vector $\boldsymbol{\chi}$ [29]:

$$\begin{aligned} \dot{\boldsymbol{X}} &= \boldsymbol{f}(\boldsymbol{X}(t), \boldsymbol{T}, t) \\ \boldsymbol{\chi}(\boldsymbol{X}_0, \boldsymbol{X}_f, t_0, t_f) &= \boldsymbol{0}, \end{aligned} \tag{6}$$

where **X** is the state vector, containing positions and velocities, while the thrust **T** is selected as control variable. The subscripts *0* and *f* indicate the values assumed by **X** at the initial and final time, respectively.

The objective is to maximize the spacecraft final mass, expressed as a merit index J, thereby minimizing the fuel consumption along the trajectory:

$$J = m_f. \tag{7}$$

According to the indirect approach, the problem is augmented by associating each variable of the state vector to an adjoint variable, contained in the costate vector $\boldsymbol{\lambda} = \{\boldsymbol{\lambda_r}, \boldsymbol{\lambda_V}, \boldsymbol{\lambda}_m\}^T$. Therefore, the design vector is composed by the previous state vector and the adjoints:

$$\bar{\boldsymbol{X}} = \begin{bmatrix} \boldsymbol{X} \\ \boldsymbol{\lambda} \end{bmatrix}, \tag{8}$$

with an overbar denoting the augmentation.

The merit index, written in the Mayer's formulation, is also augmented as follows:

$$\bar{J} = J + \boldsymbol{\nu}^T \boldsymbol{\chi} + \int_{t_0}^{t_f} \boldsymbol{\lambda}^T (\boldsymbol{f} - \dot{\boldsymbol{X}}) dt, \tag{9}$$

through the Lagrange multipliers vector $\boldsymbol{\nu}$ and the costates. In this way, if the dynamics and constraints are satisfied, maximizing the augmented parameter $\bar{J}$ coincides with optimizing the original one J.

The Hamiltonian function $H = \boldsymbol{\lambda}^T \boldsymbol{f}$ takes the form:

$$H = \boldsymbol{\lambda}_r^T \boldsymbol{V} + \boldsymbol{\lambda}_V^T \left[\boldsymbol{g}(\boldsymbol{r}) + \boldsymbol{h}(\boldsymbol{V}) + \frac{\boldsymbol{T}}{m} \right] - \lambda_m \frac{T}{c}. \tag{10}$$

This is where the Pontryagin's Maximum Principle (PMP) is invoked; the final mass is maximized by finding the optimal control (i.e. the thrust) that, per each point of the trajectory, maximizes the Hamiltonian at that precise point. Thus, the following control equation should hold:

$$\left(\frac{\partial H}{\partial \boldsymbol{T}} \right)^T = 0. \tag{11}$$

Such optimal law establishes the necessary conditions under which the control policy, resulting from the implemented method, is indisputably deemed optimal rather than suboptimal.

In this case, since the Hamiltonian is linear (or *affine*) with respect to the control $\boldsymbol{T}$, a *bang-bang* control technique is employed. By grouping all terms multiplying the thrust variable in the Hamiltonian of equation (10), the Switching Function (SF) emerges:

$$S_F = \frac{|\boldsymbol{\lambda_V}|}{m} - \frac{\lambda_m}{c}. \tag{12}$$

The thrust must be modulated along the trajectory as follows; it is maximized, $T = T_{max}$, when $S_F > 0$, while it is imposed null, $T = 0$, when $S_F \leq 0$, thus defining the entire control strategy [30, 31].

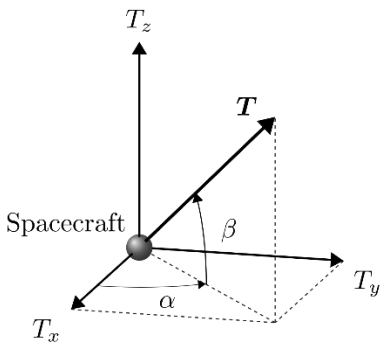

Fig. 2. Thrust angles in the synodic reference frame.

As regards the thrust directions, the cosine directors are retrieved by means of the *primer vector* $\boldsymbol{\lambda_V}$ [32]:

$$\begin{aligned} \cos\alpha \ \cos\beta &= \frac{\lambda_{\dot{x}}}{|\boldsymbol{\lambda_V}|} \\ \sin\alpha \ \cos\beta &= \frac{\lambda_{\dot{y}}}{|\boldsymbol{\lambda_V}|} \\ \sin\beta &= \frac{\lambda_{\dot{z}}}{|\boldsymbol{\lambda_V}|}, \end{aligned} \tag{13}$$

where α and β are respectively the in-plane and the out-of-plane thrust angles.

The transversality and optimality conditions, derived by maximizing the merit index ($\delta \bar{J} = 0$), dictate the behavior of trajectory for both times and states at the extremes of domain:

$$\frac{\partial J}{\partial t_0} + \boldsymbol{\nu}^T \frac{\partial \boldsymbol{\chi}}{\partial t_0} - H_0 = 0 \tag{14}$$

$$\frac{\partial J}{\partial t_f} + \boldsymbol{\nu}^T \frac{\partial \boldsymbol{\chi}}{\partial t_f} + H_f = 0 \tag{15}$$

$$\frac{\partial J}{\partial \boldsymbol{x}_0} + \boldsymbol{\nu}^T \frac{\partial \boldsymbol{\chi}}{\partial \boldsymbol{x}_0} + \boldsymbol{\lambda}_0^T = \boldsymbol{0} \tag{16}$$

$$\frac{\partial J}{\partial \boldsymbol{x}_f} + \boldsymbol{\nu}^T \frac{\partial \boldsymbol{\chi}}{\partial \boldsymbol{x}_f} - \boldsymbol{\lambda}_f^T = \boldsymbol{0}. \tag{17}$$

The Euler-Lagrange equations, instead, delineates the evolution of adjoint variables over time:

$$\frac{d\boldsymbol{\lambda}}{dt} = -\left(\frac{\partial H}{\partial \boldsymbol{x}} \right)^T, \tag{18}$$

the problem-specific form of which is reported in Appendix A.

At the implementation level, the single-shooting procedure starts by defining an initial guess $\boldsymbol{q_r} = \bar{\boldsymbol{X}}_{\boldsymbol{0}}$ for the design vector. The error in boundary conditions is computed between the values at the r-th iteration and the successive ones through a first-order Taylor expansion:

$$\boldsymbol{\chi}(\boldsymbol{q}_{r+1}) = \boldsymbol{\chi}(\boldsymbol{q}_r) + \left[\frac{\partial \boldsymbol{\chi}(\boldsymbol{q}_r)}{\partial \boldsymbol{q}_{r+1}} \right] (\boldsymbol{q}_{r+1} - \boldsymbol{q}_r). \tag{19}$$

If the solution exists, $\boldsymbol{\chi}(\boldsymbol{q}_{r+1}) = \mathbf{0}$, making it possible to retrieve the state of the design vector $\boldsymbol{q}$ at each iteration:

$$\boldsymbol{q}_{r+1} = \boldsymbol{q}_r - \left[\frac{\partial \boldsymbol{\chi}(\boldsymbol{q}_r)}{\partial \boldsymbol{q}_{r+1}}\right]^{-1} \boldsymbol{\chi}(\boldsymbol{q}_r). \quad (20)$$

The calculation proceeds iteratively until the optimal initial guess $\boldsymbol{q}^*$, which allows to reach the desired final state while fulfilling the imposed constraints, $\boldsymbol{\chi}(\boldsymbol{q}^*) = 0$, is achieved.

The Jacobian matrix $\boldsymbol{G}$, approximated via forward finite-differences methods, enables the differential correction process:

$$\boldsymbol{G}(\boldsymbol{\chi}_r, \boldsymbol{q}_{r+1}) = \frac{\partial \boldsymbol{\chi}(\boldsymbol{q}_r)}{\partial \boldsymbol{q}_{r+1}}. \quad (21)$$

where for brevity $\boldsymbol{\chi}_r = \boldsymbol{\chi}(\boldsymbol{q}_r)$. This matrix behaves as a State Transition Matrix, which is crucial in understanding how small changes in $\boldsymbol{q}$ affect the problem, and thereby how to correct the guess after each iteration.

The integration of problem equations (6) relies on the Adams-Moulton numerical approach, an implicit and linear multistep method with variable step size and order [33]. Specifically, the algorithm implements the LSODA Python integrator, known for its stability and robust- ness, making it well-suited to handle stiff differential equations [34]. In addition, the code is precompiled in C++ language, significantly enhancing computational capabilities while maintaining the flexibility and ease of use of Python. On a standard 2.80 GHz CPU laptop with an i7 Intel Core processor, LSODA proves particularly effective, achieving convergence with computation times of 1 hundredth of second per iteration and an error tolerance of 1×10^{-7}. This precision, combined with the inherent speed of the indirect method, allows for the calculation of multiple solutions in a very short time frame.

To improve the code efficiency, two numerical techniques are implemented. Firstly, a relaxation parameter κ_1 is introduced during the correction:

$$\boldsymbol{q}_{r+1} = \boldsymbol{q}_r - \kappa_1 \left[\boldsymbol{G}(\boldsymbol{\chi}_r, \boldsymbol{q}_{r+1})\right]^{-1} \boldsymbol{\chi}_r, \quad (22)$$

where $\kappa_1 = 1 \times 10^{-3} \div 1 \times 10^{-5}$. Usually, lower values are suitable during the initial assumptions for unknown variables, whereas higher values can be chosen only when the solution is reasonably close to the optimal one. Secondly, let be $E_{max} = max\, \chi_i$ the code required precision. A control on boundary conditions is imposed at the end between the error at each iteration and the subsequent one:

$$E_{max,r+1} < \kappa_2\, E_{max,r} \quad (23)$$

with $\kappa_2 = 2 \div 3$. The latter parameter is effective in facilitating the convergence of first step, even tough the first couple of steps increase the maximum error while establishing the proper optimality direction in the search space. If the error becomes significantly large, then the equation (23) does not hold and a bisection method is applied on the correction up to five times. After that, the process is automatically stopped since it is unable to converge from the selected attempt solution.

The core of the analysis, therefore, involves searching for the optimal guesses for costates that allow the spacecraft to thrust in preferential directions and correct the trajectory while satisfying all imposed constraints. The complexity of the CR3BP model makes this research more challenging, as the solution may exhibit unexpected numerical behaviors and thrust discontinuities due to the combined gravitational effects. Indeed, when the switching function oscillates around zero changing its sign multiple times during the integration, the automatic sequence of thrust-coast phases may be compromised, leading to the elimination of a desired thrust phase or to the introduction of an unwanted coast phase. Moreover, if a solution is on the border between two different switching families, for example a two-burn (T-C-T) and a three-burn (T-C-T-C-T) structure, the switching function may oscillate indefinitely without converging.

3. Boundary conditions

The case study is perfectly framed by introducing all the boundary conditions characterizing the lunar transfers. This includes reporting the features of the spacecraft and the selected engine, as well as the initial conditions for departure from Earth and the terminal conditions to insert into DRO.

3.1 Spacecraft propulsion system

To overcome the physical limitations of traditional chemical propulsors, which have low specific impulses (at best, $I_{sp} = 350 \div 450$ s), Electrical Propulsion (EP) is preferred. EP thrusters are characterized by very high I_{sp}, on the order of thousands of seconds, depending on the engine's operating principle, whether electro-thermal, electrostatic, or electromagnetic. On the other hand, these devices produce lower accelerations over time, necessitating an effective ΔV greater than the ideal one and thus extending thrust phases for hours, days, or even weeks. Since the goal of this analysis is solely to preserve propellant, irrespective of mission duration, engine efficiency is crucial. Other considerations regarding eclipse periods, during which solar power supply ceases, are beyond the scope of this study.

Several EP thrusters have been developed and tested over the past decades; however, none of these have been used as a reference since their applications are usually limited to small correction maneuvers. For a complete Earth-Moon transfer, an ideal electrostatic thruster with rather optimistic specifications has been selected. These characteristics, including engine's

specifications and the initial mass of the spacecraft, are provided in Table 3. Thrust and specific impulse are considered constant, resulting in the bang-bang control previously discussed.

The relationship between mass consumption and ΔV, namely the cost of maneuvering, is expressed by the Tsiolkovsky equation:

$$\Delta V = -I_{sp} g_0 \ln\left(\frac{m_f}{m_0}\right), \tag{24}$$

with $c = I_{sp} g_0$, where the term g_0 is the gravitational acceleration.

The burned propellant mass, which generally constitutes around $10 \div 15\%$ of the initial mass, is retrieved by difference:

$$m_p = m_f - m_0. \tag{25}$$

Table 3. Spacecraft characteristic properties.

Quantity	Value	Unit
m_0	1000	kg
I_{sp}	3000	s
T	1.0	N

3.2 Initial conditions

To accurately define an Earth-to-Moon transfer, a proper selection of the initial and final conditions is essential. While the final points of the orbit are well-known, the challenge arises with the initial point, the state of which, especially the velocities, is unknown regardless of the selected location.

Leveraging the lack of a preferential direction of integration over time, the trajectory is integrated backward in time, starting from the DRO and arriving near Earth. Therefore, by reversing the integration time, the initial point of this integration will coincide with the target of the trajectory, while the final point will provide the departure point of the transfer itself.

To a first approximation, the trajectory is computed by integrating equations (1) without considering any thrust correction, resulting in only a reference trajectory. The perilune of DRO, at $y = 0$, is selected as the initial condition for the integration and has the state:

$$\{1.180, 0.000, 0.000, 0.000, -0.498, 0.000\}^T.$$

A grid-search method is employed to identify the final (nondimensional) $\Delta \boldsymbol{V}_f$ components along the $\hat{\boldsymbol{x}}$ and the $\hat{\boldsymbol{y}}$ directions, which, combined, allow the insertion maneuver. As a result, the final velocities $\dot{x}$ and $\dot{y}$ have to be increased by:

$$\Delta \boldsymbol{V_f} = \begin{bmatrix} 0.100 \\ -0.500 \end{bmatrix}. \tag{26}$$

The integration time, which is negative, is gradually increased until the final point of the trajectory is within a certain distance from Earth, set to 20000 km. So, by integrating backward for 5.695 days, one has the point:

$$\{-0.008, -0.052, 0.000, 5.980, -0.241, 0.000\}^T,$$

which can be considered as a generic point on a circular parking MEO with a radius of 20000 km, used to leave Earth. The integrated trajectory is represented in Figure 3, where the radii of Earth and Moon are multiplied by a scale factor of 1000 for representation purposes.

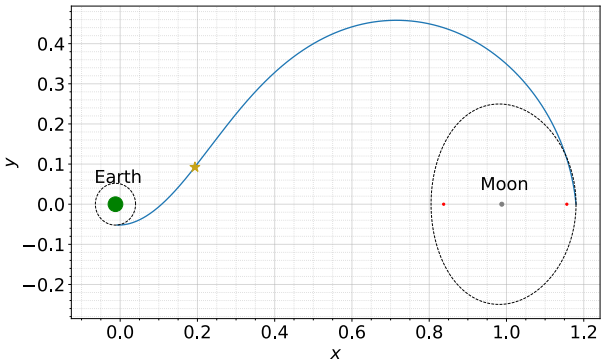

Fig. 3. Lunar transfer integrated backward over time.

However, since the code shows high sensitivity even to very small variations in velocity near Earth, it is preferred to break the trajectory, concentrating corrections only in the second part of the transfer. In other words, this strategy exploits manually the same principle behind a multi-point boundary value problem, where the trajectory is automatically divided into multiple arcs. This breakpoint, marked with a yellow star on the plot, is obtained by cutting off the integration time to 5.4 days:

$$\{0.194, 0.092, 0.000, 1.635, 2.004, 0.000\}^T.$$

Consequently, the initial mass m_0 has to change, taking into account the fuel burned during the first half. Again, from the Tsiolkovsky equation, one has:

$$m_0' = m_0\, e^{-\frac{\Delta V_0}{c}} = 944.65 \text{ kg}, \tag{27}$$

where the superscript $'$ indicates the residual mass after the first segment and will be omitted henceforth for clarity. The ΔV_0 coincides with the difference between the starting velocity on the trajectory and the circular velocity on MEO:

$$\Delta V_0 = |\boldsymbol{V}_0| - V_{MEO} = 1.674\ 0 \text{ km/s}. \tag{28}$$

This new initial mass and the state of breakpoint now represent the real initial conditions $\boldsymbol{X}_0$ for the optimization problem:

$$\boldsymbol{X}_0 = \{0.194, 0.092, 0.000, 1.635, 2.004, 0.000, 1.000\}^{\mathrm{T}},$$

where the last unit value is exactly the mass, which is nondimensionalized by the spacecraft mass itself.

To ensure the process converges, these quantities must be accompanied by seven reasonable adjoint variables, associated to initial mass, position and velocities, which are unknown. While some demonstrate a perceivable progression over time, others exhibit a less predictable behavior. The magnitude of a specific costate indicates the relevance of the corresponding state variable at the same moment in time. Adjoint velocities play a key role, as they emphasize the importance of each thrust direction with respect to the others; the sign of each adjoint indicates whether its thrust component aligns (if positive) or opposes (if negative) the direction of that velocity.

Given the form assumed by the SF in this analysis, the velocity and position costates impact directly the correction procedure by influencing the slope and level of the SF itself, respectively. Specific guesses must be selected based on the expected behavior of the SF, so that the optimal values can be identified iteratively. In this case, the adjoint variables λ_x and λ_y are both set to 1×10^{-1}, while $\lambda_{\dot{x}}$ and $\lambda_{\dot{y}}$ can be imposed in the range $1 \times 10^{-2} \div 1 \times 10^{-3}$. The λ_z and $\lambda_{\dot{z}}$ guesses are less relevant since the scenario is entirely planar. However, the high delicacy of the code prevents using null values, thus small non-zero initial values are fixed equal to 1×10^{-7}. Finally, λ_m, indicator of the spacecraft mass, is set around 1.

3.3 Terminal conditions

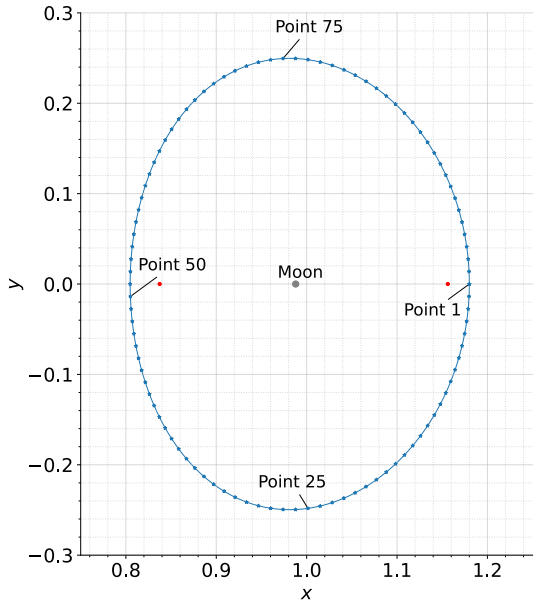

Fig. 4. Selected final points on DRO.

For fixed initial conditions, each transfer trajectory is uniquely distinguished by its final conditions. In this regard, the DRO is discretized into 100 different points, for which positions and velocities are known. Once the convergence for a specific final point is achieved, one can proceed to others using a continuation strategy to identify the optimal trajectory. Specifically, given the dynamics of the problem, the range of interest is from *point 97* to *point 24*.

Since the code proves to be extremely sensitive to changes in the Hamiltonian, the FTDC procedure is employed. Starting from the period of the integrated trajectory, the integration time is manually increased to allow corrections until convergence. As a consequence, the application of the PMP ensures the optimality of the solution only for that specific time. Such limitation is mitigated as much as possible by exploring different times for each solution in hundredths of a day to avoid falling into a suboptimal trajectory.

The reduced set of terminal boundary conditions is:

$$\boldsymbol{\chi}_f = \{x_f, y_f, z_f, \dot{x}_f, \dot{y}_f, \dot{z}_f, \Delta t\}^{\mathrm{T}}, \tag{29}$$

where Δt is the integration time for the transfer optimization. Please note that the time of flight will now be measured starting from the breakpoint, therefore, 0.2954 days must be added to retrieve the effective time.

3. Fixed-time transfer trajectories

First off, a fixed-time sensitivity analysis is conducted for the first obtained convergence. In this case, convergence is reached with a transfer time of 7.1 days, targeting the same final point of the integrated trajectory (i.e. the point at $y = 0$), referred as *point 1*. Different values of Δt are investigated in the neighborhood of these 7.1 days to evaluate the impact of assigned time on the solution. Figure 5 clearly shows how the structure of switching function and the fuel consumption change at varying of time of flight.

Under the same conditions, no convergence is achieved for shorter times than 7.1 days, as the spacecraft has too little time and thrust to appropriately correct the trajectory and complete the transfer. All the SFs belong to the same family; they exhibit a two-burn structure, consisting of an initial thrust phase to orient the trajectory, a coasting phase, and a final thrust phase to achieve the orbit insertion (T-C-T scheme). Steeper slopes of SF involve longer coasting phases, which may lead the satellite in a free-dynamic condition. To take back the trajectory on a controlled track, stronger corrections are required in the residual time, resulting in a more significant fuel consumption, with an almost linear trend.

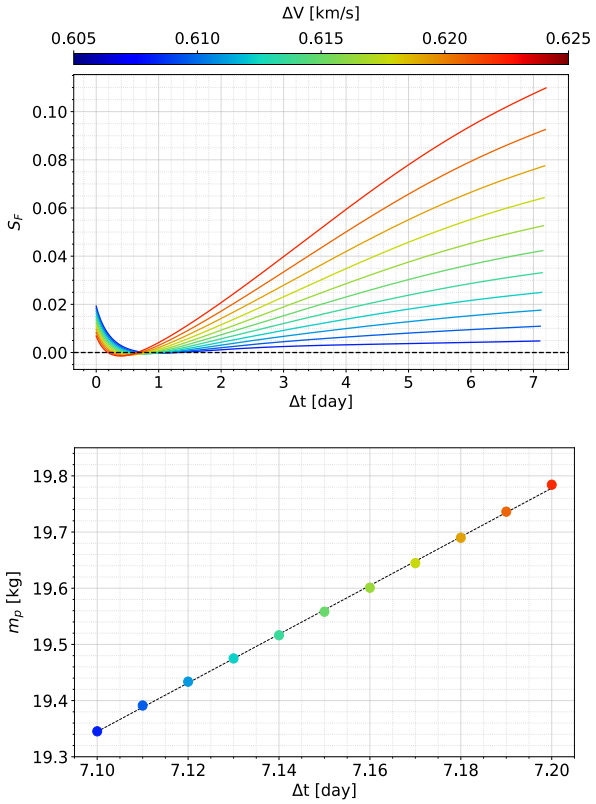

Fig. 5. SF structure and burned propellant mass for different Δt at *point 1*.

For this reason, the evolution of the in-plane angles α for these initial trajectories is reported in Figure 6. All the coasting phases occurs between 0.2 and 1.3 days.

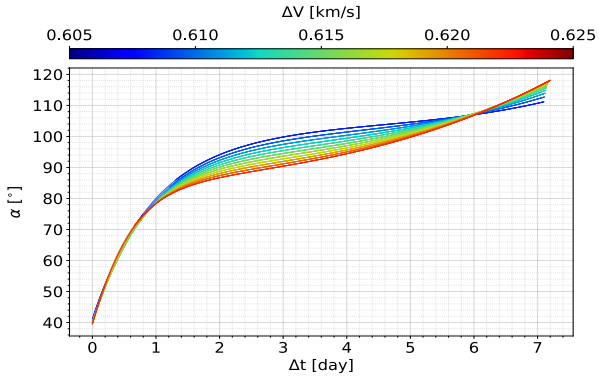

Fig. 6. Evolution of in-plane angles α over time for different Δt at *point 1*.

The solution at minimum propellant requests ends up coinciding with the one at minimum time, exactly at 7.1 days. For longer durations, the insertion trajectory slightly deviates from the optimal condition, causing the code to thrust in different directions, even if unnecessarily. After the coasting phase, the trajectory tends to curve less outward and increase the spacecraft tangential velocity, before recovering in the final part.

During this segment, the thrust opposes the spacecraft's forward motion almost parallelly, slowing it down just enough for the DRO insertion. Moreover, it is worth remembering that in the CR3BP, due to existing perturbations, there are predefined trajectories for a given energy value, namely the ZVS, deviating from which may require additional propellant.

The continuation strategy starts from here; similar reasonings are applied to the other points as well, searching for the solution at minimum time and consumption per each targeted point. By varying the final point on DRO and the relative fixed time, the entire family of solutions emerges. In Figure 7, all the resulting transfer trajectories are plotted in the $\hat{\boldsymbol{x}} - \hat{\boldsymbol{y}}$ plane as a function of the total ΔV utilized. A particular focus on the targeted points on orbit is also provided.

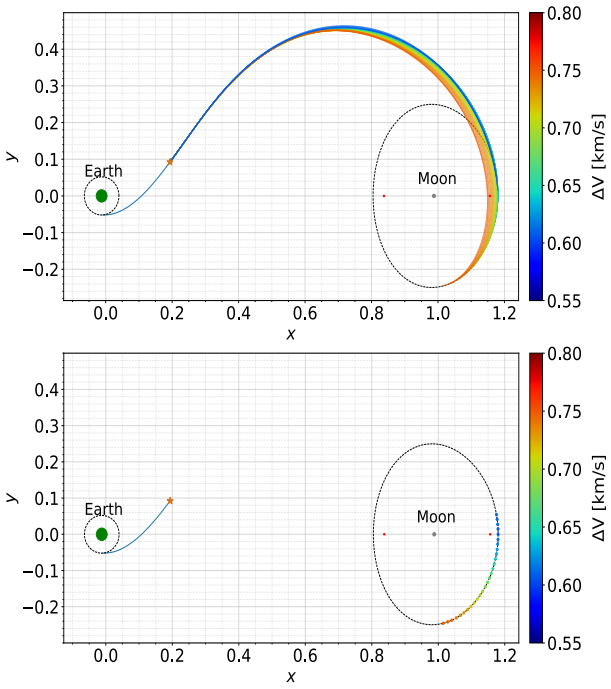

Fig. 7. Transfer trajectories for all targeted points on DRO in the $\hat{\boldsymbol{x}} - \hat{\boldsymbol{y}}$ plane.

As previously mentioned, the concentration is on a limited area of interest on the final DRO. Concerning points at negative y, it is not practical to proceed beyond *point 24*, as the required ΔV only increases. The trends of SF, besides, are increasingly flattening, indicating a gradual transition to another family, specifically to a five-phase structure (T-C-T-C-T). On the other side, solutions beyond *point 97* show a considerable increase in the slope of SF, while still maintaining a two-burn structure. Targeting these points implies transfers at the shortest times, increasing the difficulties in achieving convergence with the provided thrust values.

The diverse behavior of $y > 0$ solutions is also reflected in the evolution of guesses over time (Figure 9). Particularly, while for λ_x, λ_y, and $\lambda_{\dot{x}}$ such curves follow the longer-time solutions, for $\lambda_{\dot{y}}$ they rise sharply, similar to what is observed for the switching functions. This is because the guess $\lambda_{\dot{y}}$ is associated with the most significant variable of the problem -i.e. the $\dot{y}$ velocity-, which directly influences the primer vector in SF. The trends of λ_z and $\lambda_{\dot{z}}$, instead, stabilize at zero throughout the entire integration time. In order to respect the imposed optimality conditions, $\lambda_{\dot{z}}$ values gradually increase to 1.

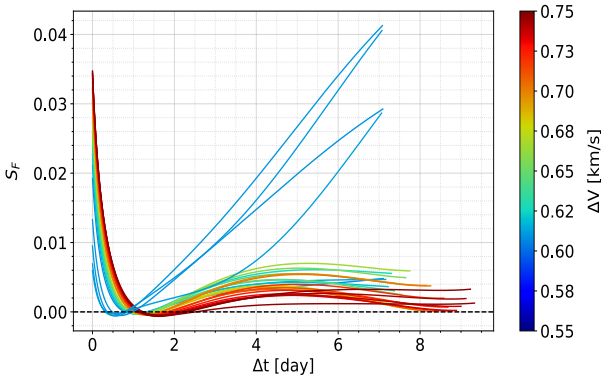

Fig. 8. SF structures for all trajectories. Shortest-time solutions stand out for their slopes.

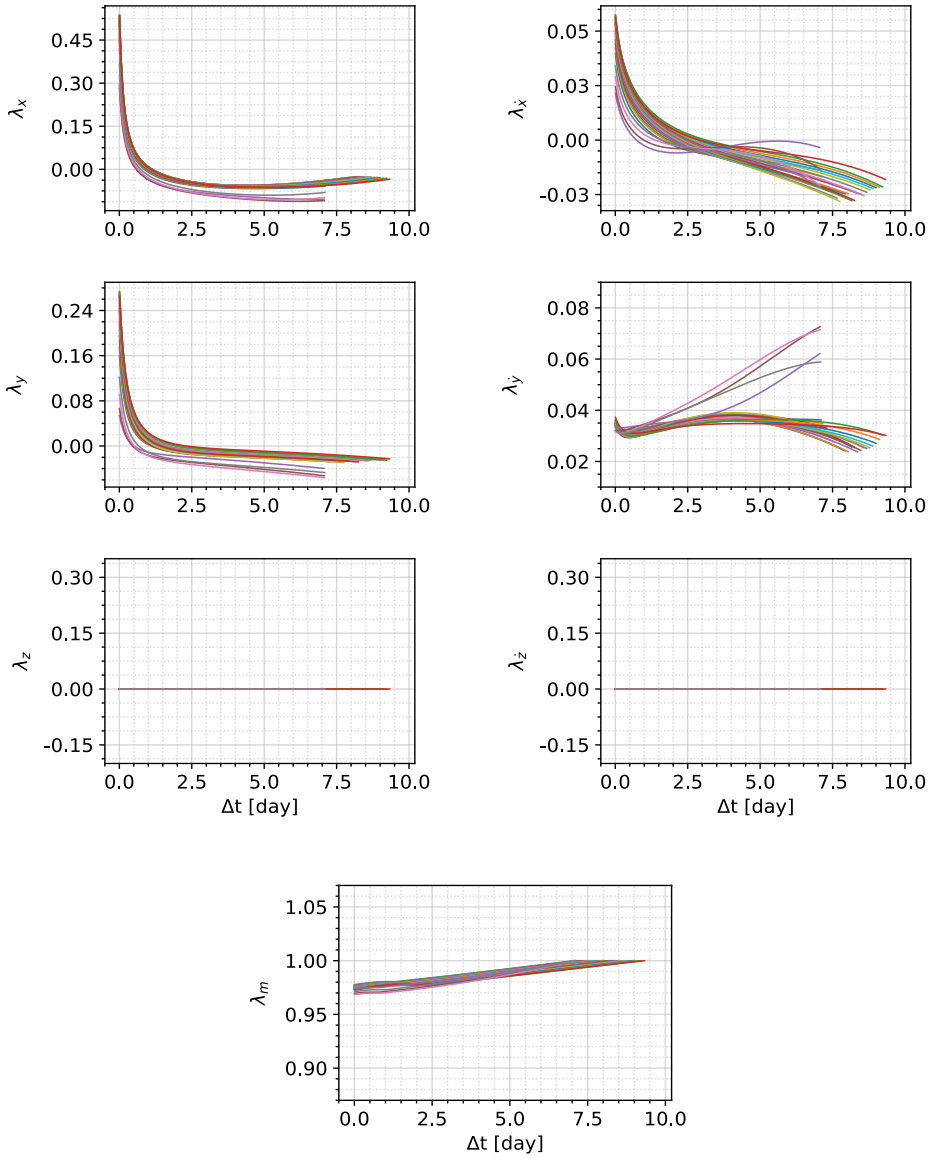

Fig. 9. Evolution of guesses

The variation in the assigned time of flight is reported in Figure 10 below. Each final point is expressed in percentage of position along the orbit, where *point 1* corresponds to 0%.

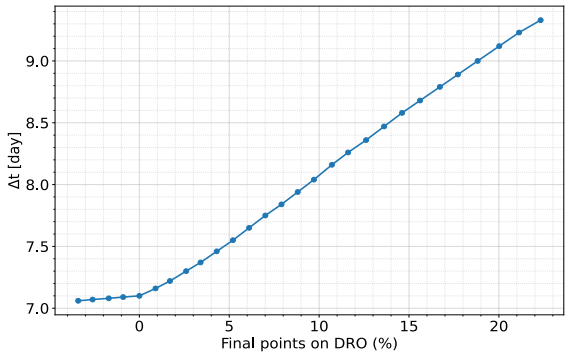

Fig. 10. Fixed time of flight Δt for each solution.

It is easy to observe that, following the irregular shape of the DRO and targeting progressively more distant points, the assigned Δt values exhibit a perfectly linear trend, as one might expect. Once again, the resistance encountered in converging the solutions for $y > 0$ leads to a more cautious and gradual allocation of times, which explains the slightly lower slope of the initial segment.

Proceeding to $y < 0$ results in longer thrusting phases and increasingly higher propellant mass requests (Figure 11), where, as usual, the relationship between m_p and ΔV is described by the Tsiolkovsky equation. Counterintuitively, a shorter transfer does not necessarily mean a lower consumption. For positive y values, while the transfer time decreases, fuel consumption begins to increase again since the thrust phases must be sufficient within the limited time available. This increase is slightly mitigated by the easier achievement of the tangency condition between the trajectory and the orbit. Indeed, the optimal trajectory better suits the quasi-elliptical shape of the DRO by inserting the spacecraft with a velocity that is as aligned as possible with the orbit velocities. Higher thrust values would be necessary to explore other solutions, both in terms of arc structure and insertion point on the DRO.

As expected, the optimal trajectory proves to be the one at minimum time that least deviates from the integrated trajectory, specifically the one that targets *point 1*. This point ensures a perfectly tangential insertion at $\dot{x} = 0$, with a consumption of "only" 19.35 kg:

$$\boldsymbol{X}_f^* = \{1.180, 0.000, 0.000, 0.000, -0.498, 0.000, 925.31\}^{\mathrm{T}},$$

where $m_f^* = 925.31$ kg is the optimal value for the spacecraft final mass. The complete results are reported in Table 4.

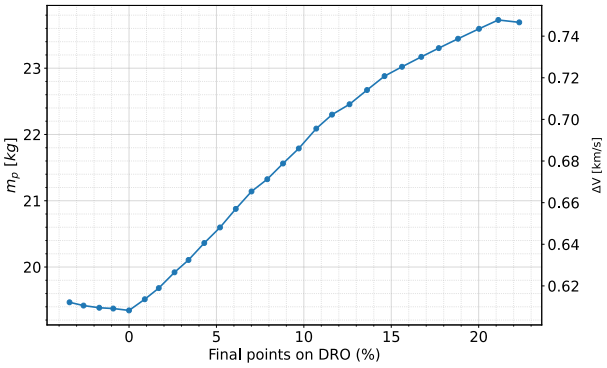

Fig. 11. Burned propellant mass (and total cost ΔV) for each solution.

Table 4. Optimal final results.

Δt^* [day]	m_f^* [kg]	m_p^* [kg]	ΔV^* [km/s]
7.1	925.31	19.35	0.608

The optimal transfer trajectory can be retrieved from the specific optimal guesses, $\{\lambda_x, \lambda_y, \lambda_z, \lambda_{\dot{x}}, \lambda_{\dot{y}}, \lambda_{\dot{z}}, \lambda_m\}^T$, reported here:

$$\boldsymbol{\lambda_0^*} = \{0.432, 0.163, 0.000, 0.040, 0.035, 0.000, 0.978\}^T.$$

The plot in Figure 13 highlights the diverse phases along the trajectory, distinguished by color depending on whether the engine is turned on ($S_F > 0$, in red) or off ($S_F < 0$, in green). This low-thrust engine requires the spacecraft to thrust for the majority of the trajectory, except during the phase from $x \approx 0.40$ to 0.51, where it coasts.

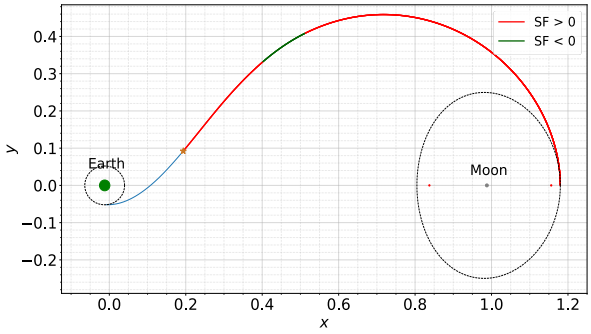

Fig. 12. Optimal transfer trajectory to *point 1*, divided into thrust phases ($S_F > 0$) and coast phases ($S_F < 0$).

As anticipated, the SF follows the T-C-T family scheme. Such structure, coupled with the evolution of the final mass over time, is displayed in Figure 13.

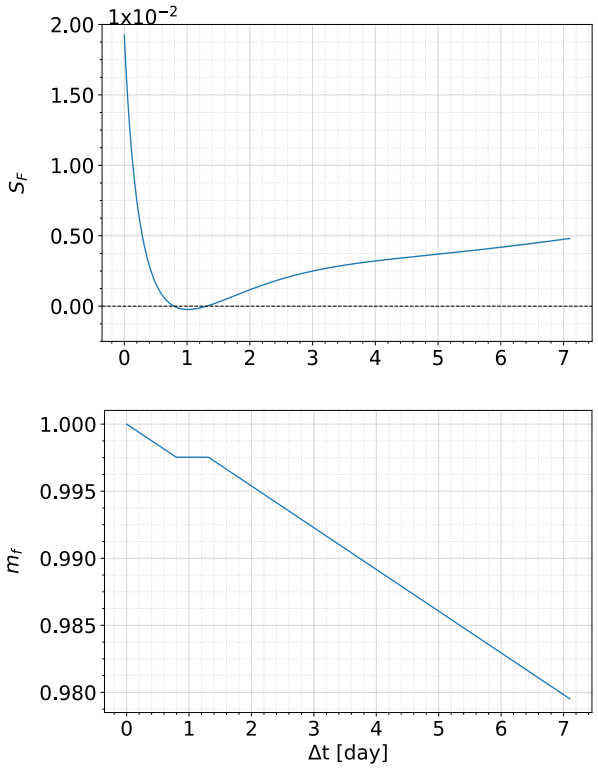

Fig. 13. Evolution of SF and spacecraft total mass fraction over time.

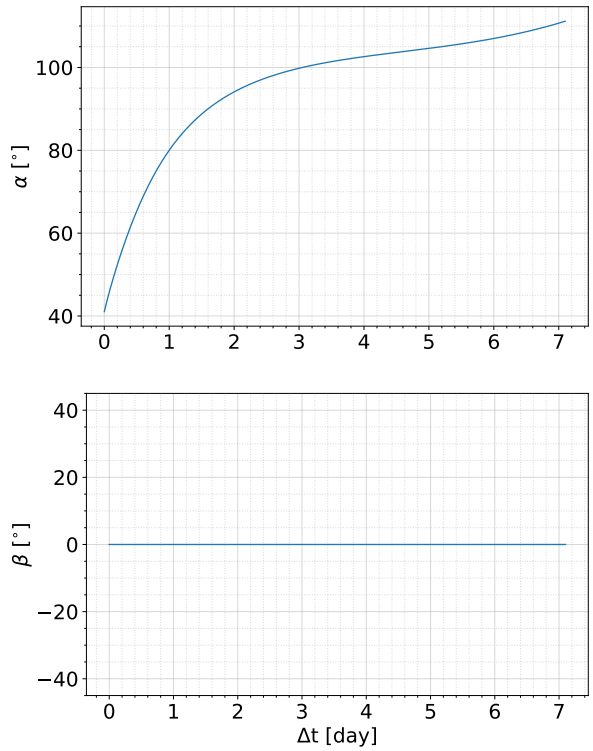

Fig. 14. Evolution of the in-plane α and out-of-plane β thrust angles over time.

The portion of the SF curve at negative values, corresponding to the coasting phase, results in a plateau at 942.32 kg in the total mass trend. It is precisely the duration of such coasting phase (from 0.33 to 1.31 days), that makes this solution stand out from the others, ensuring greater fuel savings while maintaining a controlled trajectory.

The direction of the thrust vector is not immediately apparent. For this reason, it is necessary to carefully analyze the evolution of the in-plane and out-of-plane thrust angles over time (Figure 14).

The α angle exhibits an always increasing trend. The initial values around $40 \div 50°$ determine an acceleration in the forward direction. The satellite opens the trajectory upwards, curving it just enough to allow for DRO insertion. During the second thrust phase, the angle assumes values well beyond 90°, as the spacecraft thrusts back to the front and slows down. The continuous deceleration peaks towards the end, when α reaches values around 111°, resulting in a thrust nearly opposite to the advancing trajectory. This braking completely nullifies the velocity component along the $\hat{\boldsymbol{x}}$ -axis, leading the spacecraft to the desired insertion velocities. On the other hand, the β angle is always null, as the examined scenario is entirely planar.

For completeness, the evolution of positions and velocities over time is reported in Figure 15. The trends of x and y perfectly reflect the curving of trajectory, while the velocities $\dot{x}$ and $\dot{y}$ decrease until they match those of *point 1*. Once again, the planar dynamics of the problem impose that z and $\dot{z}$ are null.

5. Conclusions

This paper focuses on optimizing low-thrust transfer trajectories to insert directly into a selenocentric DRO within the planar CR3BP. Although more challenging to implement, the indirect formulation has been identified as the most suitable for space application problems, ensuring more robust solutions and higher computational speed.

The fundamentals of OCT were applied to an iterative single-shooting algorithm, aimed at maximizing the spacecraft final mass using a FTDC scheme. To avoid suboptimal solutions, a time-sensitivity analysis was conducted for each transfer time. To handle the thrust control variable along the trajectory, a bang-bang control strategy was implemented, where the PMP allowed the validation of an optimal solution for that assigned time.

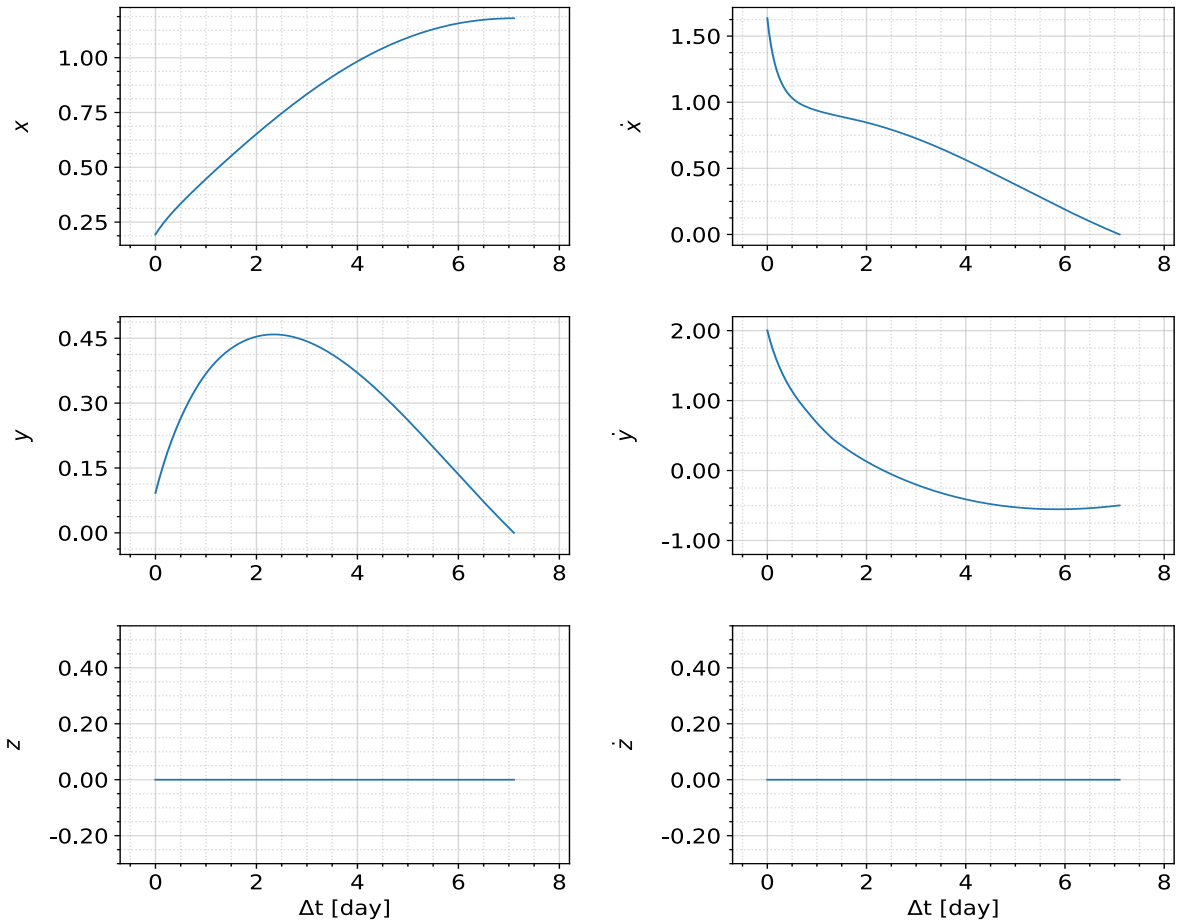

Fig. 15. Evolution of spacecraft's optimal positions $\boldsymbol{r} = \{x, y, z\}^T$ and velocities $\boldsymbol{V} = \{\dot{x}, \dot{y}, \dot{z}\}^T$ over time.

To conclude, the dual purpose of this research has thus been achieved. The implemented code has proved to be flexible and efficient, establishing a valuable baseline for identifying cost-effective trajectories in the most diverse applications. Furthermore, direct solutions to reach cislunar space, by exploiting the presence of stable, periodic DROs have been explored. Results suggest that two-burn trajectories provide the most effective approach for the orbit insertion. The optimal trajectory is the one at minimum fuel consumption, which best fits the quasi-elliptical shape of DRO in the shortest time.

5.1 Future research

Future developments may focus on addressing the limitations related to a fixed-time analysis. One promising approach is to effectively convert the TPBVP into a multi-point boundary value problem, by dividing the trajectory into multiple arcs and imposing additional boundary conditions at intermediate nodes [26]. At that stage, applying the PMP would indisputably ensure the optimality of the solution. Additionally, the challenges of the indirect method could be tackled by defining *a priori* the succession of thrust and coast phases for the entire trajectory, thus stabilizing the switching structure and guiding the solution towards optimality.

It may also be interesting to explore alternative solutions to DRO direct insertions, such as multi-revolution trajectories or transfers that exploit the contact points between DROs and tangential LOs [17]. These maneuvers could then be applied in various scenarios of imminent interest, including rendezvous with asteroids or lunar landing operations [18-21].

For better adherence to reality, the model could be transitioned from the adopted CR3BP to a higher-fidelity n-body problem. The examined POs would be converted into quasi-periodic orbits, by taking into account ephemeris data and planetary perturbations. Furthermore, variations in departure dates may significantly affect the optimized trajectories, revealing diverse behaviors based on the relative positions of celestial bodies.

Acknowledgements

This study was developed as a part of a Master's thesis at the Politecnico di Torino. The achieved results

would not have been possible without the guidance and the supervision of Dr. Luigi Mascolo.

Appendix A

A.1 Euler-Lagrange equations

$$\dot{\lambda}_x = -\lambda_{\dot{x}}\left[1-\frac{1-\mu}{r_{13}^3}+\frac{3(1-\mu)(x+\mu)^2}{r_{13}^5}+ -\frac{\mu}{r_{23}^3}+\frac{3\mu(x-1+\mu)^2}{r_{23}^5}\right]+ -\lambda_{\dot{y}}\left[\frac{3(1-\mu)(x+\mu)y}{r_{13}^5}+\frac{3\mu(x-1+\mu)y}{r_{23}^5}\right]+ -\lambda_{\dot{z}}\left[\frac{3(1-\mu)(x+\mu)z}{r_{13}^5}+\frac{3\mu(x-1+\mu)z}{r_{23}^5}\right] \quad (30)$$

$$\dot{\lambda}_y = -\lambda_{\dot{x}}\left[\frac{3(1-\mu)(x+\mu)y}{r_{13}^5}+\frac{3\mu(x-1+\mu)y}{r_{23}^5}\right]+ -\lambda_{\dot{y}}\left[1-\frac{1-\mu}{r_{13}^3}+\frac{3(1-\mu)y^2}{r_{13}^5}-\frac{\mu}{r_{23}^3}+\frac{3\mu y^2}{r_{23}^5}\right]+ -\lambda_{\dot{z}}\left[\frac{3(1-\mu)yz}{r_{13}^5}+\frac{3\mu yz}{r_{23}^5}\right] \quad (31)$$

$$\dot{\lambda}_z = -\lambda_{\dot{x}}\left[\frac{3(1-\mu)(x+\mu)z}{r_{13}^5}+\frac{3\mu(x-1+\mu)z}{r_{23}^5}\right]+ -\lambda_{\dot{y}}\left[\frac{3(1-\mu)yz}{r_{13}^5}+\frac{3\mu yz}{r_{23}^5}\right]+ -\lambda_{\dot{z}}\left[-\frac{1-\mu}{r_{13}^3}+\frac{3(1-\mu)z^2}{r_{13}^5}-\frac{\mu}{r_{23}^3}+\frac{3\mu z^2}{r_{23}^5}\right] \quad (32)$$

$$\dot{\lambda}_{\dot{x}} = -\lambda_x - 2\lambda_{\dot{y}} \quad (33)$$

$$\dot{\lambda}_{\dot{y}} = -\lambda_y + 2\lambda_{\dot{x}} \quad (34)$$

$$\dot{\lambda}_{\dot{z}} = -\lambda_z \quad (35)$$

$$\dot{\lambda}_m = \frac{T}{m^2}\lambda_V \quad (36)$$

References

[1] R.A. Broucke, *Periodic orbits in the restricted three body problem with earth-moon masses*. No. JPL-TR-32-1168 (1968).

[2] M. Hénon, *Generating families in the restricted three-body problem*, Astronomy and Astrophysics, vol. 52, Springer Science & Business Media, 1997.

[3] M. Hénon, *Numerical exploration of the restricted problem. V*, Astronomy and Astrophysics, 1 (1969) 223-238.

[4] M. Hénon, *Numerical exploration of the restricted problem. VI. Hill's case: non-periodic orbits*, Astronomy and Astrophysics, 9 (1970) 24-36.

[5] M. Hénon, *Vertical stability of periodic orbits in the restricted problem. I. Equal masses*, Astronomy and Astrophysics, 28 (1973) 415.

[6] M. Hénon, *Vertical Stability of Periodic Orbits in the Restricted Problem. II. Hill's Case*, Astronomy and Astrophysics, 30 (1974) 317-321.

[7] C.A. Ocampo, and G.W. Rosborough, *Transfer trajectories for distant retrograde orbiters of the Earth*, NASA STI/Recon Technical Report A, 95 (1993) 1323-1337.

[8] R. Whitley and R. Martinez, *Options for staging orbits in cislunar space*, Aerospace Conference, IEEE, 2016.

[9] C. Bezrouk and J.S. Parker, *Long term evolution of distant retrograde orbits in the Earth-Moon system*, Astrophysics and Space Science, 362 (2017) 1-11.

[10] C. Bezrouk and J.S. Parker, *Long duration stability of Distant Retrograde Orbits*, AIAA/AAS astrodynamics specialist conference, San Diego, California, 2014, 4-7 August, p. 4424.

[11] M. Gates and D. Mazanek, *Asteroid Redirect Mission (ARM)*, 15th Meeting of the NASA Small Bodies Assessment Group, Johns Hopkins University Applied Physics Laboratory: Lunar and Planetary Institute, Baltimora, Maryland, 2016, 28-30 June.

[12] NASA, *Orion Will Go the Distance in Retrograde Orbit During Artemis I*, 18 April 2022, https://www.nasa.gov/missions/orion-will-go-the-distance-in-retrograde-orbit-during-artemis-i/, (accessed 20.11.23).

[13] J. Foust, *Orion enters lunar Distant Retrograde Orbit*, 25 November 2022, https://spacenews.com/orion-enters-lunar-distant-retrograde-orbit/, (accessed 20.11.23).

[14] T.F. Dawn, J. Gutkowski, A. Batcha, J. Williams, and S. Pedrotty, *Trajectory design considerations for exploration mission 1*, Space Flight Mechanics Meeting, (2018) 968.

[15] A.L. Batcha, J. Williams, T.F. Dawn, J.P Gutkowski, M.V. Widner, S.L. Smallwood, B.J. Killeen, E.C. Williams, and R.E. Harpold, *Artemis I trajectory design and optimization*, AAS 20-649, AAS/AIAA Astrodynamics Specialist Conference, South Lake Tahoe, California, 2020, 9-13 August.

[16] X. Ming and X. Shiijie, *Exploration of distant retrograde orbit*, Acta Astronautica, 65.5-6 (2009) 853-860.

[17] C.M. Welch, J.S. Parker, and C. Buxton, *Mission considerations for transfers to a distant retrograde orbit*, The Journal of the Astronautical Sciences, 62 (2015) 101-124.

[18] J. Demeyer and P. Gurfil, *Transfer to distant retrograde orbits using manifold theory*, Journal of Guidance, Control, and Dynamics, 30.5 (2007) 1261-1267.

[19] G. Mingotti, F. Topputo, and F. Bernelli-Zazzera, *Transfers to distant periodic orbits around the Moon via their invariant manifolds*, Acta Astronautica, 79 (2012) 20-32.

[20] L. Capdevila, D. Guzzetti, and K. Howell, *Various transfer options from Earth into distant retrograde orbits in the vicinity of the Moon*, 24th AAS/AIAA Space Flight Mechanics Meeting, vol. 118, Santa Fe, New Mexico, 2014.

[21] R. Zhang, Y. Wang, H. Zhang, and C. Zhang, *Transfers from distant retrograde orbits to low lunar orbits*, Celestial Mechanics and Dynamical Astronomy, 132 (2020) 1-30.

[22] N. Murakami, and K. Yamanaka, *Trajectory design for rendezvous in lunar Distant Retrograde Orbit*, IEEE Aerospace Conference, (2015) 1-13.

[23] D. Conte, M. Di Carlo, K. Ho, D.B. Spencer, and M. Vasile, *Earth-Mars transfers through Moon distant retrograde orbits*, Acta Astronautica, 143 (2018) 372-379.

[24] D. Conte, and D.B. Spencer, *Mission analysis for Earth to Mars-Phobos distant retrograde orbits*, Acta Astronautica, 151 (2018) 761-771.

[25] V. Szebehely, *Theory of Orbits: The Restricted Problem of Three Bodies*, Academic Press Inc, New York, 1967.

[26] C. Zhang, F. Topputo, F. Bernelli-Zazzera, and Y. Zhao, *Low-Thrust Minimum-Fuel Optimization in the Circ Circular Restricted Three-body Problem*, Journal of Guidance, Control, and Dynamics, 38.8 (2015) 1501-1510.

[27] R.E. Pritchett, *Numerical methods for Low-Thrust Trajectory Optimization*, PhD thesis, Purdue University, West Lafayette, Indiana, 2016.

[28] P.J. Roache, and P.M. Knupp. *Completed Richardson extrapolation*, Communications in Numerical Methods in Engineering, 9.5 (1993) 365-374.

[29] J.T. Betts, *Survey of numerical methods for trajectory optimization*, Journal of guidance, control, and dynamics, 21.2 (1998) 193-207.

[30] L. Mascolo, *Low-Thrust Optimal Escape Trajectories from Lagrangian Points and Quasi-Periodic Orbits in a High-Fidelity Model*, PhD thesis, Politecnico di Torino, Turin, 2023.

[31] A. Zavoli, *Indirect Optimization of Bang-Bang Control Problems and Applications to Formation Flying Missions*, PhD thesis, Università La Sapienza di Roma, Rome, 2013.

[32] D.F. Lawden, *Optimal trajectories for space navigation*, Butterworths & Co. (Publishers) Ltd., 1963.

[33] L.F. Shampine, and M.K. Gordon, *Computer solution of ordinary differential equations: the initial value problem*, Freeman, San Francisco, 1975.

[34] SciPy Community, *Scipy.integrate.LSODA*, 2024, https://docs.scipy.org/doc/scipy/reference/generated/scipy.integrate.LSODA.html, (accessed 20.11.2023).